Chapter 9 Quantum Phase Transition in $Ba_{(1-x)}Ca_xFe_{12}O_{19}$

9.1 Introduction

Classical phase transitions (CPT), like boiling of water, are ubiquitous in nature and affect our day-to-day life. They occur at a finite transition temperature (T_c) as a result of a competition between the energy of the low temperature phase and the entropy fluctuations with an energy scale of k_BT. Quantum phase transitions (QPT), on the other hand, occur at the quantum critical point (QCP) $T_c = 0$ K (absolute zero) as a result of the competition between the energy of the system and the quantum fluctuations of energy scale $\hbar\omega$, where ω is the zero-point vibrational frequency of quantum oscillator. Although the QCP ideally occurs at absolute zero temperature which is not experimentally realizable, its remarkable impact on several exotic phenomena occurring at finite temperatures (e.g. high temperature superconductivity, metal insulator transition, integer and fractional Hall effects) makes it an area of vigorous research in condensed matter and materials science [62,144,454–458]. The QCP has been located in a variety of strongly correlated [459–463] and other systems (KH_2PO_4) [464] by gradually tuning the T_c close to 0 K through non-thermal variables, like composition (x), pressure (p), electric (E) or magnetic (H) field [464–468]. The finger prints of the QPT persist above the QCP also in the so-called "quantum critical" regime also where quantum fluctuations dominate over the thermal fluctuations (i.e. $\hbar\omega > k_BT$) and give rise for example to non-classical exponents for the dependence of T_c on the non-thermal control parameters. Interestingly, Nature has provided us with a family of materials called quantum paraelectrics (QPE), like $SrTiO_3$ [49], $KTaO_3$ [52], $CaTiO_3$ [469], TiO_2 [470] and $EuTiO_3$ [471], which already possess a QCP and one can study the effect of quantum fluctuations in the

quantum critical regime by driving the system away from the QCP on application of non-thermal variables [467,472].

Very recently, in a series of publications [14,15] it has been argued that M type hexaferrites, especially the $BaFe_{12}O_{19}$ (BFO), are also QPE. First principles calculations on BFO have revealed 1D chains of electric dipoles arranged on a triangular lattice with ferroelectric (FE) and antiferroelectric (AFE) interactions along the c-axis and in the *ab*-plane, respectively, arising out of two unstable Γ point optical phonon modes [16]. On account of the AFE interactions between the neighbouring dipoles on the triangular lattice, BFO is geometrically frustrated [7,16]. The concept of frustration in the field of ferroelectrics and relaxors is not new but the frustration in BFO is unique because of its geometrical nature as the previously reported systems were based on competing AFE and FE interactions [473–476]. The reports on quantum saturation of ε(T) in BFO below T ~ 10K (a canonical signature for the quantum paraelectricity) have become questionable because of the observation of an upturn in the 1/ ε'(T) versus T plot around 4 K with a $1/T^3$ like dependence of ε'(T) in agreement with the theory of uniaxial quantum paraelectrics [150]. First principles DFT calculations in conjunction with Monte-Carlo (MC) simulations using a simple dipole-dipole interaction model also suggest the possibility of a phase transition at T_c ~ 3 K to a geometrically frustrated antiferroelectric (AFE) state [16]. The complex interplay of geometrical frustration and quantum fluctuations in BFO offers tremendous potential for the discovery of new exotic states of matter with phenomenological similarities with their magnetic counterparts [62,142,144,361,477,478] notwithstanding the intrinsic differences in the microscopic origin and dynamics of electrical and magnetic dipoles [7]. In fact, it has already been proposed that the exotic quantum spin liquid like state involving electric dipoles may exist in BFO at very low temperatures [7].

In this chapter, we have investigated the effect of a non-thermal variable, namely chemical pressure and local electric field, generated through substitution of Ba^{2+} with a much smaller isovalent ion Ca^{2+}, on the quantum critical behaviour of BFO using dielectric and specific heat measurements from 1.66 K to 100 K and 1.8 K to 300 K, respectively. We observe a cusp in the dielectric permittivity of BFO at $T_c \sim 2.91$ K with negative Curie-Weiss (Θ_{cw}) temperature expected for antiferroelectric (AFE) correlations, in excellent agreement with the theoretical predictions [16]. By analysing the specific heat data with and without magnetic field, we have found evidence for excess specific heat of non-Debye and non-magnetic origin which is approximately linear in T below T_c = 2.91 K supporting the possibility of a QEDL state at low temperatures in agreement with the earlier report based on thermal conductivity measurements [7]. The T_c of BFO is shown to increase with increasing Ca^{2+} content (x) in the $(x - x_c)^{1/2}$ manner, characteristic of phase transitions in the quantum critical regime [56,467,479,480] in marked contrast to the $T_c \sim (x - x_c)$ type dependence expected for the classical regime [56,467]. Our dielectric results reveal that $Ba_{(1-x)}Ca_xFe_{12}O_{19}$ (BCFO-x) does not exhibit long range ordered AFE ground state, but may correspond to QEDL like state for pure BFO (x = 0), and quantum dipole glass state with frustrated AFE interactions for higher Ca^{2+} content ($x \geq 0.03$). This QEDL state coexist with the spin-glass state of BFO discussed in preceding chapters.

9.2 Experimental

Synthesis details of BFO is given in chapter 2. However, Ca^{2+} doped BFO were synthesized by the solid state thermo-chemical reaction route using analytical reagent grade chemicals: $BaCO_3$ (≥ 99.0% assay, Sigma Aldrich), Fe_2O_3 (≥ 99.0% assay, Sigma Aldrich) and $CaCO_3$ (≥ 99.5% assay, Alfa Aesar). Stoichiometric mixture of chemicals were mixed properly using an agate mortar and pestle for 3 hours followed by ball milling

in zirconia jar and balls which acted as the grinding medium. Acetone was used as a milling medium. Mixing was done for 12 hours. The sample was dried at room temperature after mixing. Calcinations were carried out in alumina crucibles. The Ca^{2+} doped samples were calcined at 1523 K for 6 hours. The calcined powders were further crushed using mortar and pestle**.** Then a few drops of 2% Polyvinyl Alcohol (PVA) were added to it as a binder. Pellets were made using cylindrical steel die and uniaxial hydraulic press machine. Pellets were kept at 873 K for 10 hours to remove the PVA. All the Ca^{2+} doped samples were sintered at 1548 K for 1 hour.

Room temperature synchrotron X-ray diffraction (SXRD) data were collected at a wavelength of 0.207150Å at P02.1 beamline in Petra III, Hamburg, Germany. For the SXRD measurements, the powder used was obtained from sintered pellets which were crushed into fine powders and then annealed at 873 K for 10 hours to remove the stresses introduced during crushing.

For dielectric measurements, the top and bottom surfaces of the sintered pellets were mildly polished using diamond paste. After polishing, the pellets were kept in isopropyl alcohol to remove moisture and then electroded using fired-on (773 K for 2 minutes) silver paste. Low temperature dielectric permittivity of BFO was measured for all the samples using a fully computer-controlled measuring system involving Novo Control Alpha-A High Frequency Analyzer and a cryogen free measurement system (CFMS). First the measurements were carried out in the range 1.66 K to 100 K at a heating rate 0.3 K per minute at a fixed frequency of 300 kHz. This was followed by dielectric measurements over the temperature range 1.66 K to 25 K at multiple frequencies in the range 10 kHz to 400 kHz.

For heat capacity measurements, a small piece of sintered pellet was used after annealing at 873 K for 10 hours. The heat capacity measurement of BFO was carried out

using a Physical Properties Measurement System DynaCool (Quantum Design). The annealed piece of the sintered pellet was mounted on the sample platform inside the puck using apiezone N-grease. The apiezone N-grease is used for better thermal conduction between sample and platform of the puck. First, we have carried out the addenda (heat capacity measurement of platform + apiezone N-grease). After that, heat capacity measurement of sample (i.e. sample + platform + apiezone N-grease) was performed. The absolute value of the heat capacity of the sample was obtained by subtracting the value of heat capacity of addenda from the total measured heat capacity.

9.3 Results and Discussion

9.3.1 Evidence for chemical pressure generated by Ca^{2+} substitution

Room temperature crystal structure of BFO is hexagonal in the space group $P6_3/mmc$ [118,119]. The unit cell of BFO can be visualized in terms of stacking of S and R blocks in the sequence RSR*S* (asterisk (*) marked blocks here represent in new atomic position within the block after rotating it through 180^0 about the hexagonal axis w.r.t. the new atomic in the initial block) as shown in Fig. 9.1(a). The S block contains two close-packed layers of oxygen whereas the R block consists of three close packed layers of oxygen in a hexagonal close packed arrangement with one oxygen in the middle layer being replaced with Ba. Oxygen atoms in the hexagonal unit cell occupy 4e, 4f, 6h, 12k, 12k Wyckoff positions. The Ba atoms go to the Wyckoff site 2d. Fe atoms occupy five different Wyckoff sites 2a, $4f_2$, 12k (octahedral sites), $4f_1$ (tetrahedral site) and 2b (trigonal bi-pyramidal (TBP)) site as can be seen from Fig. 9.1(b). At room temperature, the Fe spins are ferromagnetically coupled within the "*ab*"- plane but the spins at 2a, 2b, 12k sites are antiparallel to those at the $4f_1$, $4f_2$ sites in the *c* direction. Since the number of up (16 spins) and down (8 spins) spins are unequal, BFO shows an Ising type collinear ferrimagneitc ordering of spins [39] with a large net magnetic moment of $20\mu_B$ per

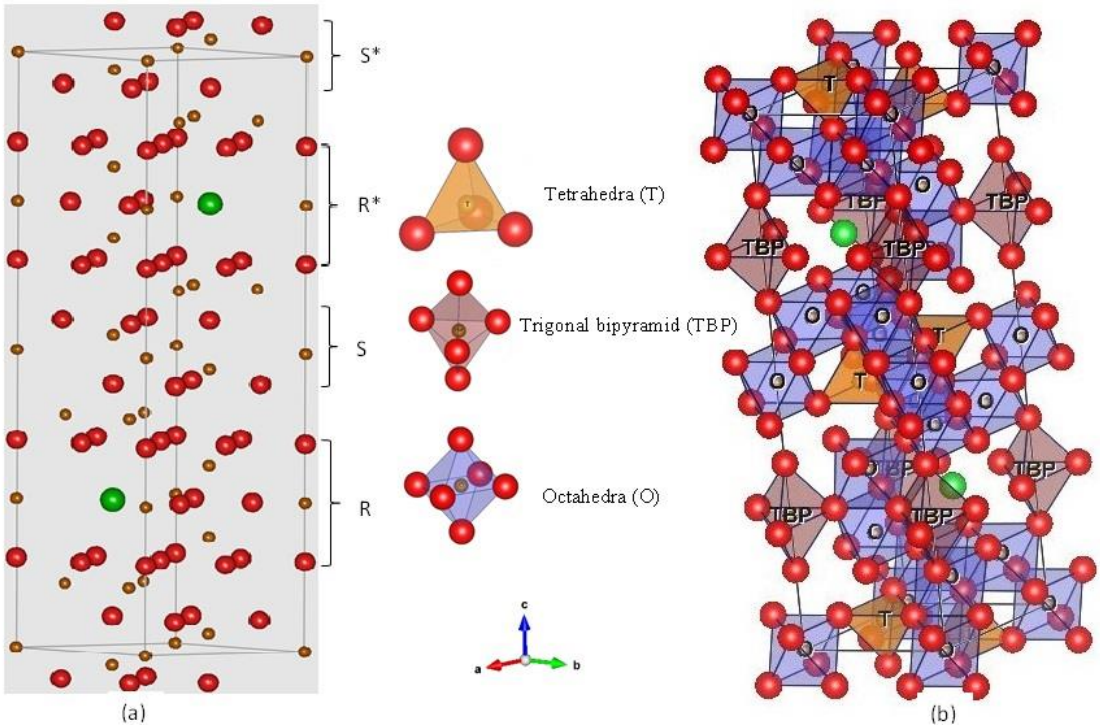

Figure 9.1: (a) Unit cell of M-Type hexaferrite. (b) Polyhedra of the M-type unit cell

formula unit and a Curie temperature of T_c = 723 K. At room temperature, x-ray and neutron as well as first principles studies have revealed that Fe^{3+} ion does not sit at the centre of the TBP (at the 2b site) but is displaced away from a mirror plane to the 4e sites along the *c*-axis. But this off-centre displacement cannot be captured on the basis of Rietveld refinements and accordingly we have placed Fe atom in the TBP coordination at the 2b site [15,16,119].

Since Ca^{2+} ion is much smaller in size than the Ba^{2+}, it is expected to generate positive chemical pressure and the unit cell volume should accordingly decrease with increasing Ca^{2+} content (x). To confirm this, we carried out Rietveld refinement using SXRD data for various composition of BCFO-x. The positional coordinates of the atoms in the asymmetric unit used in the refinement are: 2/3, 1/3, 0.25 for Ba at 2d site, 0, 0, 0 for Fe1 at 2a site, 0, 0, 0.25 for Fe2 at 2b site, 1/3, 2/3, z for Fe3 at 4f1 site, 1/3, 2/3, z for Fe4 at 4f2 site, x, y, z for Fe5 at 12k site, 0, 0, z for O1 at 4e site, 1/3, 2/3, z for O2 at 4f

Table 9.1**:** Atomic positions obtained from the Rietveld refinement for different compositions.

atoms	x = 0.00	x = 0.05	x = 0.07	x = 0.10
a (Å)	5.9723(2)	5.9707(4)	5.9700(5)	5.9690(3)
c (Å)	23.540(2)	23.521(3)	23.509(3)	23.501(2)
B(Ba/Ca)	0.5(2)	0.1(1)	0.2(2)	0.3(2)
B(Fe1)	0.3(4)	0.2(5)	0.4(5)	0.4(6)
B(Fe2)	1.1(4)	1.1(6)	1.1(5)	1.4(7)
Z_{Fe3}	0.0272(6)	0.0273(8)	0.0272(7)	0.0272(7)
B(Fe3)	0.3(3)	0.1(3)	0.2(3)	0.3(4)
Z_{Fe4}	0.1904(5)	0.1904(7)	0.1904(7)	0.1904(8)
B(Fe4)	0.4(2)	0.3(3)	0.4(3)	0.4(4)
X_{Fe5}	0.168(2)	0.168(3)	0.168(3)	0.168(3)
Y_{Fe5}	0.337(4)	0.337(6)	0.337(5)	0.337(6)
Z_{Fe5}	-0.1082(3)	-0.1083(4)	-0.1083(4)	-0.1084(4)
B(Fe5)	0.5(1)	0.4(1)	0.4(2)	0.4(1)
Z_{O1}	0.151(2)	0.151(3)	0.151(2)	0.151(3)
B(O1)	0.4(1)	0.0(2)	0.3(2)	0.4(2)
Z_{O2}	-0.054(2)	-0.054(3)	-0.054(2)	-0.054(3)
B(O2)	0.2(1)	0.2(2)	0.1(2)	0.1(2)
X_{O3}	0.18(1)	0.18(1)	0.181(1)	0.180(1)
Y_{O3}	0.36(2)	0.36(3)	0.36(2)	0.361(3)
B(O3)	0.2(9)	0.1(1)	0.2(1)	0.4(1)
X_{O4}	0.156(7)	0.157(9)	0.157(9)	0.15(1)
Y_{O4}	0.31(1)	0.31(2)	0.31(2)	0.31(2)
Z_{O4}	0.051(1)	0.052(1)	0.052(1)	0.052(2)
B(O4)	0.4(6)	0.1(8)	0.2(7)	0.3(8)
X_{O5}	0.501(9)	0.50(1)	0.500(9)	0.50(1)
Y_{O5}	1.00(2)	1.00(2)	1.00(2)	1.00(2)
Z_{O5}	0.149(1)	0.149(2)	0.149(2)	0.149(2)
B(O5)	0.5(6)	0.03(9)	0.3(8)	0.034(7)
χ^2	1.13	1.12	1.47	0.785
R_{wp}	3.15	3.90	4.06	4.19
R_{exp}	2.97	3.68	3.79	4.73
Fe2-O1	2.326(5)	2.317(7)	2.315(7)	2.310(7)
Fe2-O3	1.874(5)	1.872(7)	1.871(6)	1.870(7)

site, x, y, 0.25 for O3 at 6h site, x, y, z for O4 at 12k site and x, y, z for O5 at 12k site. Table 9.1 lists the refined structural parameters for all the compositions. We have obtained excellent fits between the observed and calculated profiles after Rietveld

refinement for all the compositions. This is illustrated in Fig. 9.2 for x = 0.0, 0.05, 0.07 and x=0.10. Our Rietveld refinements confirm that the structure of BCFO-x (x > 0) remains identical to BFO (x=0), i.e. hexagonal in the $P6_3/mmc$ space group.

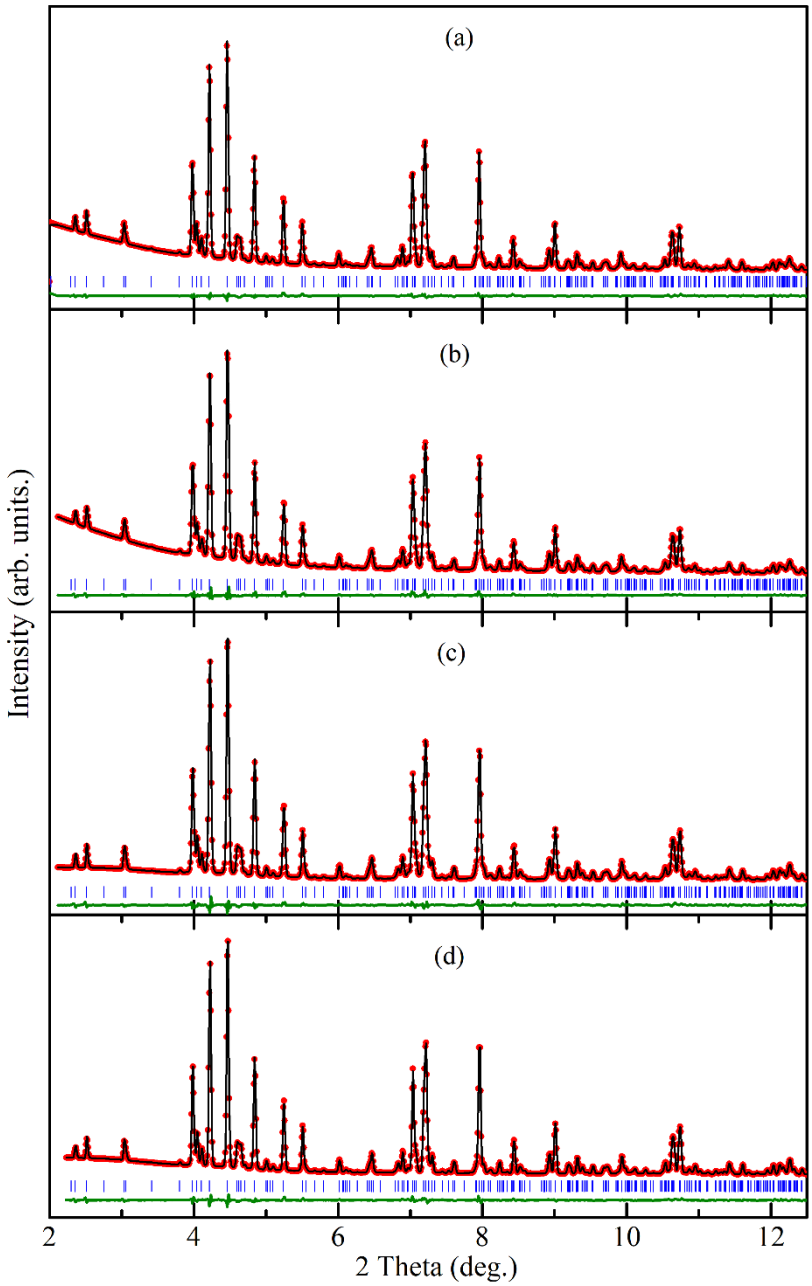

Figure 9.2: (a) Observed (red circles), calculated (black continuous line) and difference (bottom green line) profiles obtained after Rietveld refinement using $P6_3/mmc$ space group for $Ba_{(1-x)}Ca_xFe_{12}O_{19}$ with (a) x= 0, (b) x = 0.05, (c) x = 0.07 and (b) x=0.10.The vertical bars represent the Bragg peak positions (blue).

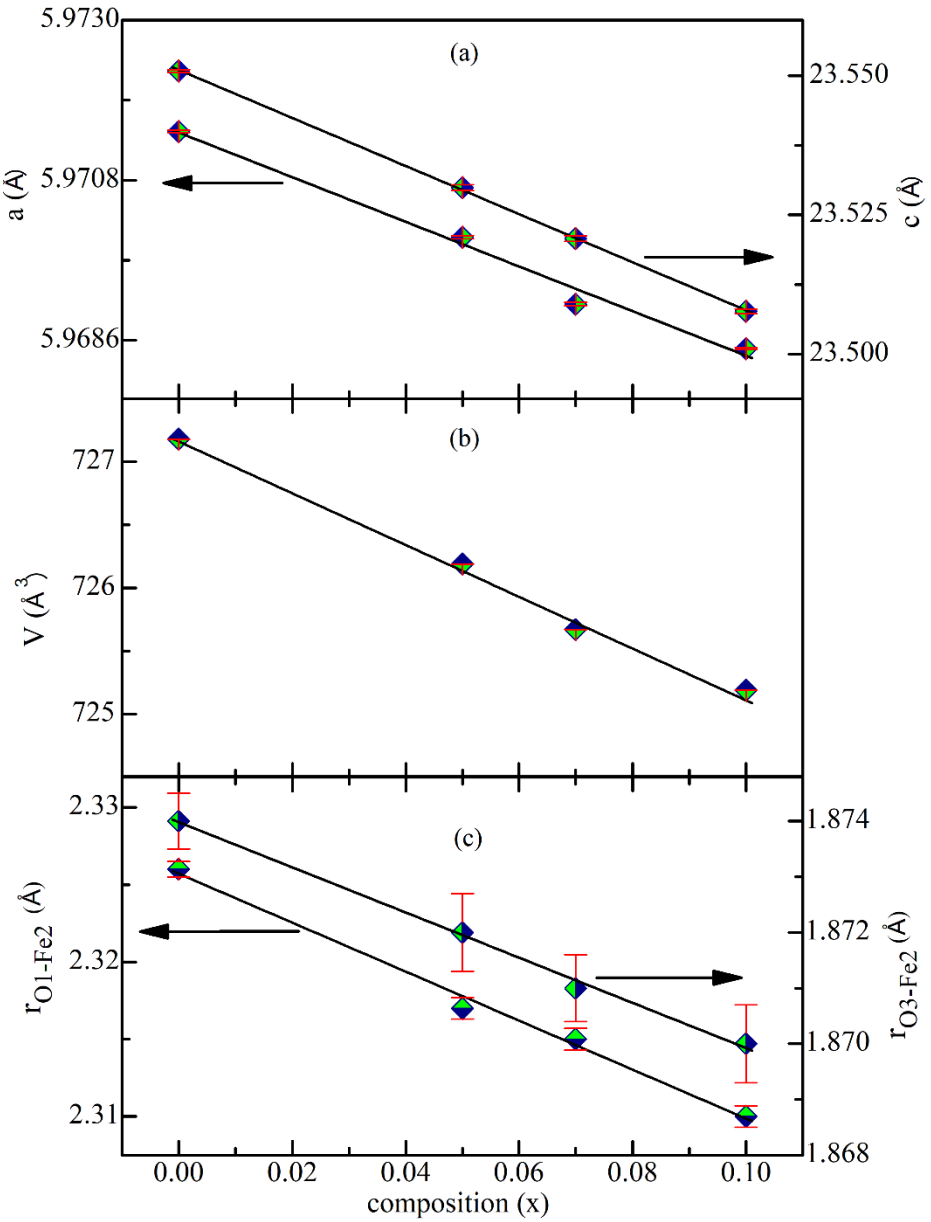

Figure 9.3: Variation of (a) lattice parameters a, c, (b) unit cell volume V and (c) bond lengths Fe2-O1 and Fe2-O3 of $Ba_{(1-x)}Ca_xFe_{12}O_{19}$ in the composition range $0 \leq x \geq 0.10$.

Figs. 9.3(a) and (b) depict the variation of lattice parameters (a, c) and unit cell volume (V) as a function of Ca^{2+} content (x), respectively. The fact that the unit cell volume decreases with increasing "x" confirms that Ca^{2+} substitution generates positive chemical pressure in the BFO matrix. In addition to generating chemical pressure, Ca^{2+} substitution may also lead to creation of local electric dipoles because the smaller ions

like Ca^{2+} have a tendency to go off-centre with respect to the Ba^{2+} site in the centre of the AO_{12} polyhedra, as is well known for Ca^{2+} doped $SrTiO_3$ (SCT) [47,467] or Li^{1+} doped $KTaO_3$ (KTL) systems [52,76,481]. We also calculated the bond lengths in the ab-plane (Fe2-O3) and along the c-axis (Fe2-O1) using Fullprof Suite [186] from the refined positional coordinates. Fig. 9.3(c) depicts their variation with x. As expected, these bond lengths also decrease with increasing Ca^{2+}content. The refined structural parameters and bond lengths for all the compositions are listed in Table 9.1.

9.3.2 Effect of Ca^{2+} Substitution on Quantum Critical Behaviour of BFO

To understand the effect of chemical pressure and local electric field due to off-centred Ca^{2+}ions on the quantum critical behaviour of BFO, we show in Fig. 9.4 the temperature dependence of the real ε'(T) and imaginary ε''(T) parts of the dielectric permittivity of BCFO-x in the temperature range 1.66 to 100 K measured at 300 kHz. It is evident from Fig. 9.4(a) that pure BFO shows a smeared dielectric response with a critical temperature T_c ~ 2.91 K which is in excellent agreement with the theoretical predictions of a transition at T_c ~ 3 K [16]. Ca^{2+} substitution enhances T_c and also makes the dielectric anomaly more prominent by increasing the peak height at the critical temperature as cam be seen from Figs. 9.4(b) to (e). These figures reveal an anomaly in both ε'(T) and ε''(T) around 18 K which is due to the presence of the second longitudinal spin-glass transition, discussed in chapter 5. This was confirmed by ac susceptibility measurements on the polycrystalline sample at 500 Hz. The results are shown in Fig. 9.5 for various compositions. These observations suggest that the second longitudinal spin-glass transition show magnetodielectric coupling. The increase in T_c seems to be primarily due to an increase in the strength of the dipole-dipole interactions both in the ab plane as well as along the c axis as a result of the contraction of the bond lengths of the FeO_5 trigonal bi-pyramids (TBPs) caused by chemical pressure generated by Ca^{2+} (see

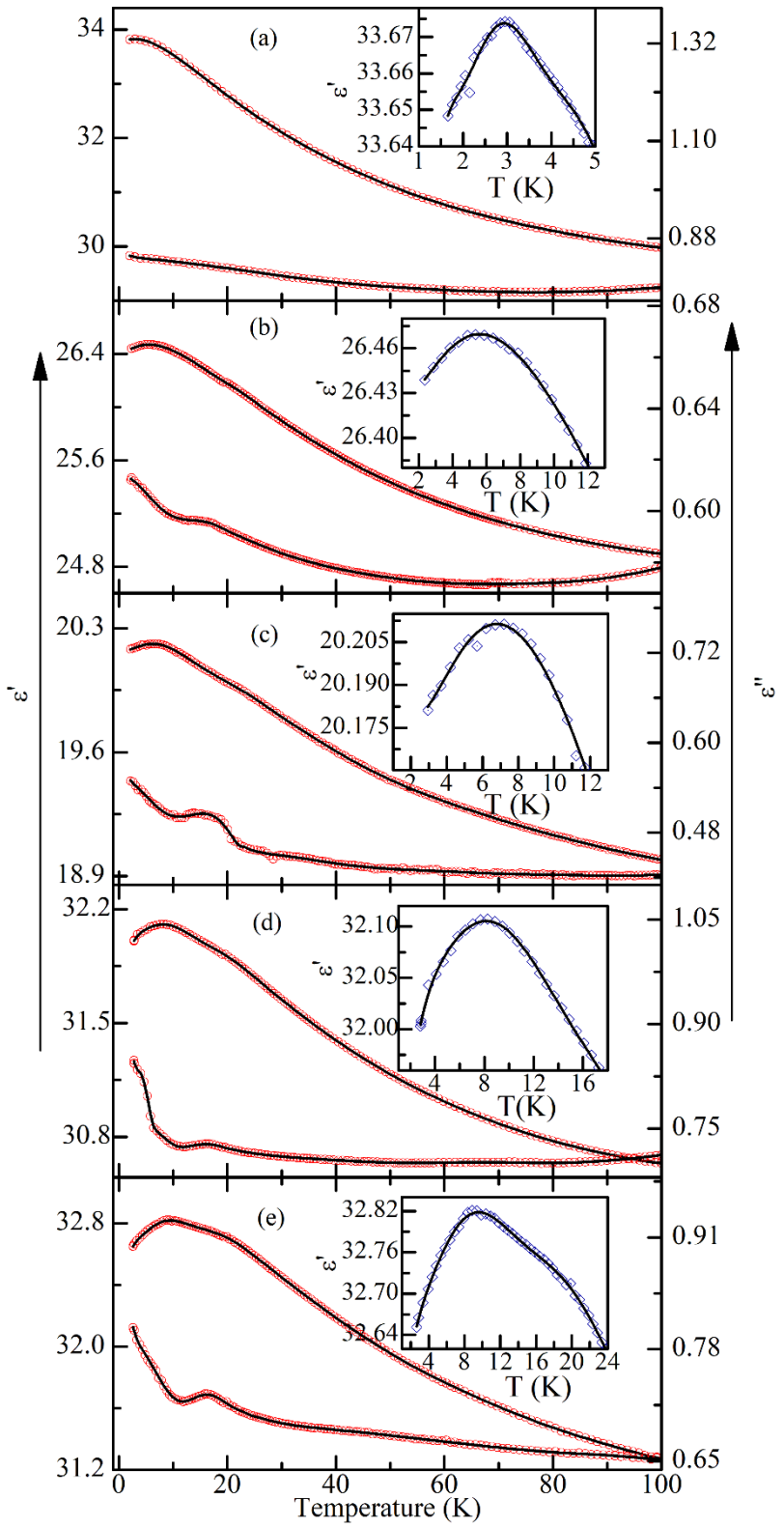

Figure 9.4: Variation of the real (ε') and imaginary (ε'') parts of the dielectric permittivity of $Ba_{(1-x)}Ca_xFe_{12}O_{19}$ at 300 kHz for different Ca^{2+} concentrations with x = (a) 0, (b) 0.03, (c) 0.05, (d) 0.07 and (e) 0.10. Insets in (a)-(e) show the variation of ε' on the zoomed scale.

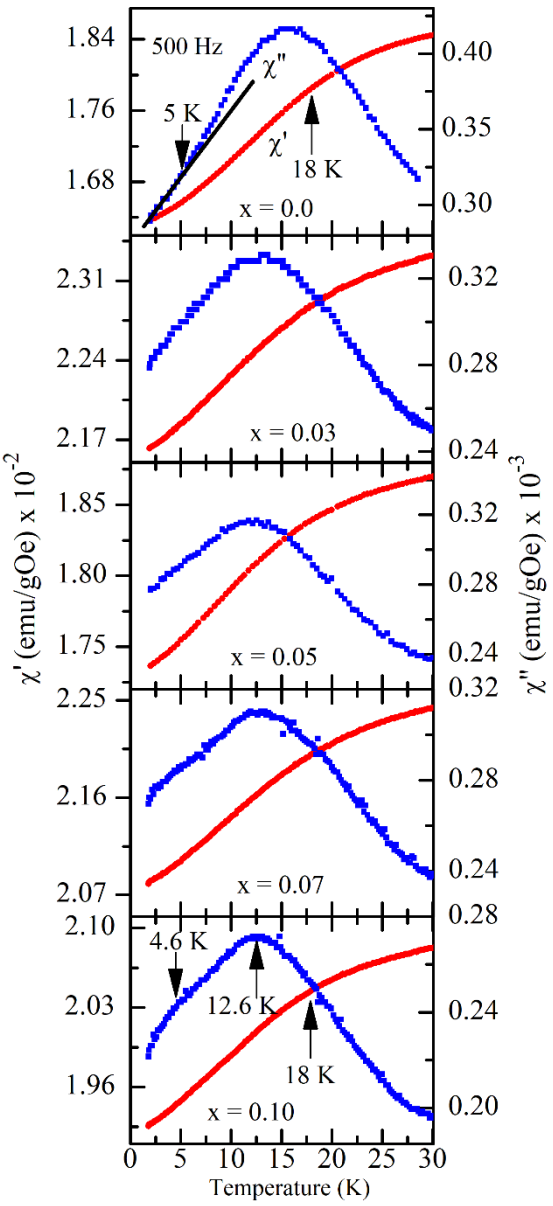

Figure 9.5: Variation of ac susceptibility of BCFO-x.

Fig. 9.3 (c)). This is consistent with the theoretical predictions also according to which external compressive stresses should in general enhance T_c [16]. The T_c in other doped quantum paraelectric systems, like SCT [467] and KTN [52,481], is known to follow $(x-x_c)^{1/2}$ type composition dependence in the quantum critical regime [56,467,480,481] in marked contrast to $(x-x_c)$ type dependence for the classical phase transitions [56,481]. The variation of T_c of BCFO-x as a function of Ca^{2+} content (x) also follows $(x - x_c)^{1/2}$

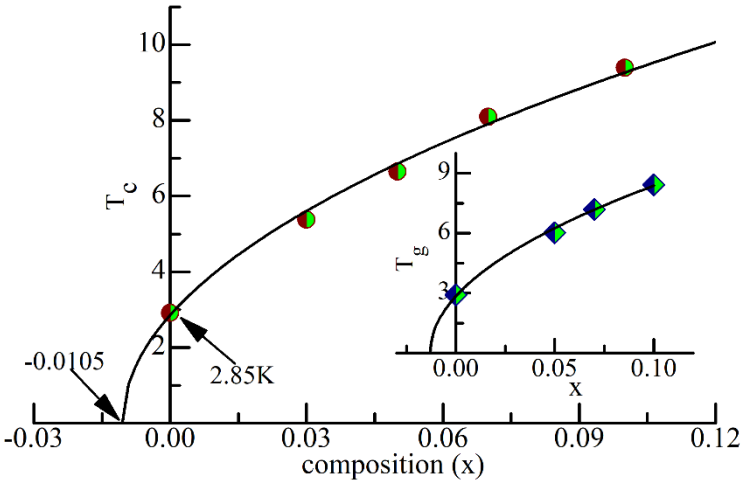

Figure 9.6: Variation of dielectric peak temperature (T_c) at 300 kHz of $Ba_{(1-x)}Ca_xFe_{12}O_{19}$ as a function of Ca^{2+} concentration (x). Inset shows variation of glass transition temperature (T_g) as a function of Ca^{2+} concentration (x).

type dependence as can be seen from Fig. 9.6. The continuous line in this figure through the data points is the least squares fit to $(x - x_c)^{1/2}$ type dependence of T_c. Interestingly, the extrapolation of the $T_c \sim (x - x_c)^{1/2}$ plot for BCFO-x to x = 0 gives a value of $T_c \sim 2.85$ K for undoped BFO in perfect agreement with the experimentally observed peak temperature $T_c = 2.91$ K shown in the inset of Fig. 9.4(a) and the theoretically predicted $T_c \sim 3$ K [16]. Further, T_c approaches 0 K on the negative side of the composition axis suggesting that negative pressure is required to locate the QCP of BFO. This is similar to the situation reported in some heavy fermion systems undergoing quantum phase transitions where QCP lies on the negative pressure axis of the phase diagram [461,482]. Such a negative pressure in BFO can be generated by substitution with a larger isovalent ion like Pb^{2+} and we predict that Pb^{2+} substitution can drive BFO closer to its QCP in contrast to Ca^{2+} which drives it away from the QCP. Our results thus reveal that BFO is very close to QCP, but its true QCP can be realised by applying negative pressure.

9.3.3 Evidence for Quantum Electric Dipole Glass State in Ca^{2+} Substituted BFO

The positive chemical pressure and/or local electric field generated by random site dipoles associated with off-centred cations are known to suppress quantum fluctuations [56] and stabilise quantum ferroelectric/ferrielectric phases in SCT [47,467] and quantum dipole glass in KLT [52,76]. Unlike the SCT and KLT systems, the geometrical frustration in Ca^{2+} doped BFO (e.g. BCFO-x) may lead to three different types of phases below the dielectric peak temperature T_c: (1) an LRO state as observed in SCT [47,467] and predicted for BFO also as in ref. [16], (2) a quantum dipole glass state with a characteristic critical dynamics showing ergodicity breaking similar to KLT [76] and (3) quantum electric dipole liquid (QEDL) state as proposed in ref. [7] for BFO. The $\varepsilon'(\omega, T)$ plots near the peak temperature T_c, measured at several frequencies (in the 40 to 400 kHz) at a very slow heating rate of 0.1 K/min, reveal considerable dispersion for all the compositions (see Fig. 9.7). Further, the temperature T'_m corresponding to the peak in $\varepsilon'(\omega, T)$ for $x \geq 0.03$ shifts to higher temperatures on increasing the measuring frequencies ($\omega = 2\pi f$). It is evident from these figures that the dielectric peak temperature shifts to higher frequencies for the doped samples only as no such shift is observed for the undoped BFO down to 500 Hz**.** However, even undoped BFO shows considerable dispersion in the value of ε' indicating highly degenerate ground state with possible low temperature tunnelling among the various states**.** Frequency dependent shift of the dielectric peak temperature is known to occur in glassy systems [52,76]. The non-linear nature of the $\ln(\tau)$ versus $1/T$ plot shown in Fig. 9.8 for $x = 0.05$ rules out Arrhenius behaviour of the relaxation time τ. A similar situation holds good for $x = 0.07$ and 0.10 also. We could model the temperature dependence of τ of all the composition for $x > 0.03$

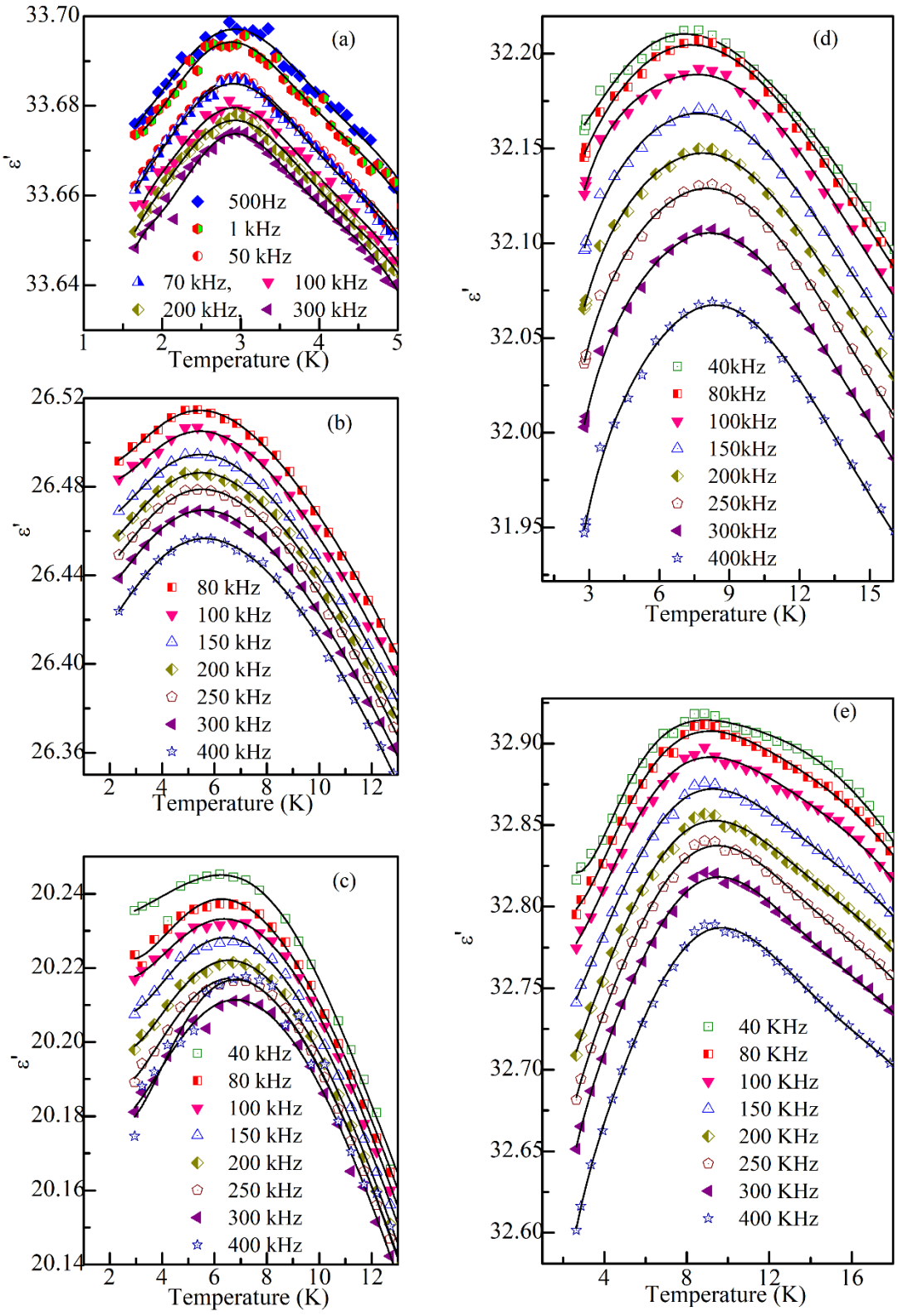

Figure 9.7: Variation of the real (ε') part of the dielectric permittivity of $Ba_{(1-x)}Ca_xFe_{12}O_{19}$ for (a) x = 0, (b) x = 0.03, (c) x = 0.05, (d) x = 0.07 and (e) x=0.10 measured at various frequencies.

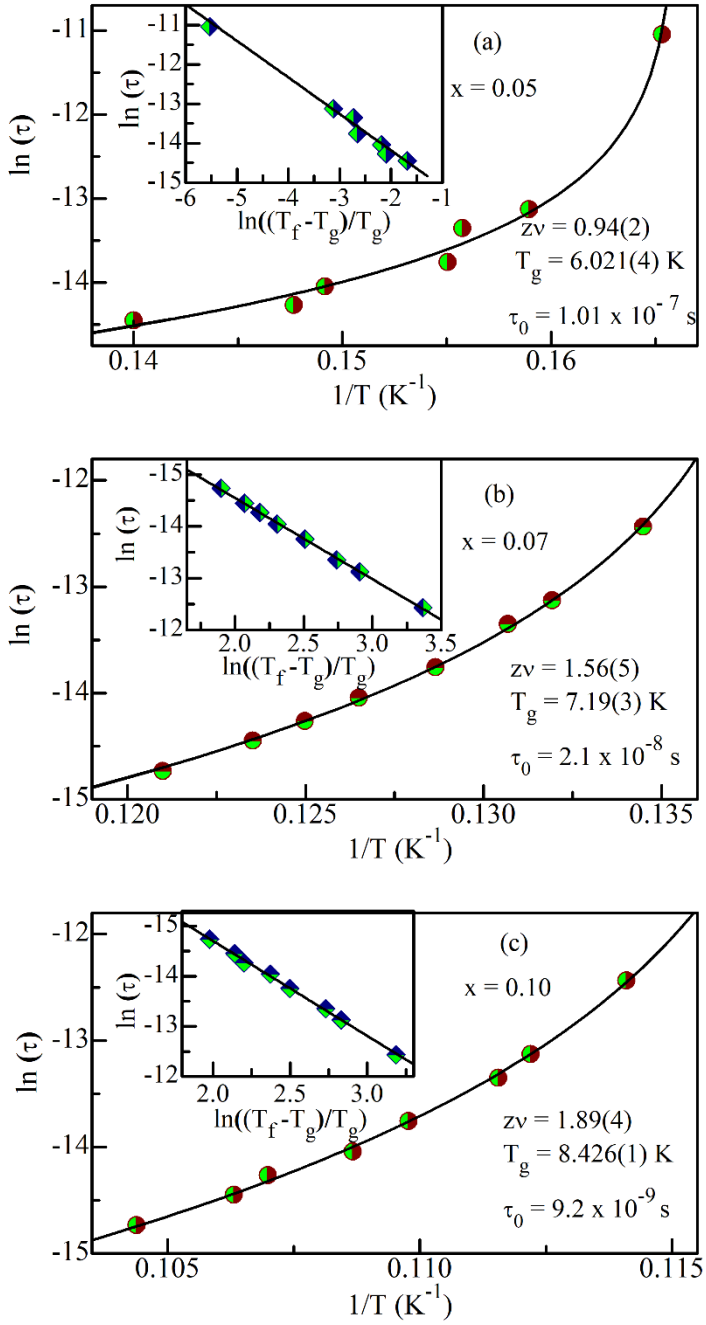

Figure 9.8: Non-Arrhenius behaviour of temperature dependence of relaxation time (τ) shown in ln(τ) versus 1/T plot of $Ba_{(1-x)}Ca_xFe_{12}O_{19}$ for (a) x=0.05, (b) 0.07 and (c) 0.10. The continuous line in insets (a)-(c) shows fit for ln(τ) vs $\ln(\frac{T_{max}-T_g}{T_g})$ plot using power law dynamics $\tau = \tau_0(\frac{T_{max}-T_g}{T_g})^{-z\nu}$ characteristic of a dipolar glass transition.

using power-law dynamics, commonly used in spin-glass systems [57,60,61]:

$$\tau = \tau_0 \left(\frac{T_f - T_g}{T_g}\right)^{-z\nu} \qquad \text{.....(9.1)}$$

where $\tau_0 = 1/\omega$ is the inverse of the attempt frequency, T_g the critical temperatures at which the slowest polar dynamics diverges signalling ergodicity breaking, z the dynamical critical exponent for the correlation length and ν the critical exponent related to the correlation length. The fit corresponding to the power-law behaviour is shown in the inset of Figs. 9.8(a), (b) and (c) for x=0.05, 0.07 and 0.10, respectively. The critical exponent increases from $z\nu = (0.94 \pm 0.002)$ to (1.89 ± 0.004) on increasing Ca^{2+} content from x = 0.05 to 0.10 but remains within the limit of canonical glasses as discussed in the context of the spin-glass systems [60]. Similarly**,** the attempt frequency also increases from 9.9 x 10^6 to 1.08 x 10^8 with Ca^{2+} content**.** Our analysis clearly shows that Ca^{2+} substitution induces a crossover from diffuse transition behaviour in BFO with $T_c \sim 2.91$ K, as evidenced by the smeared ε'(T) response for x = 0 with absence of frequency dependent shift of T_c, to a canonical quantum dipole glass phase with dielectric peak temperature shifting to higher temperature side with increasing frequency of alternating current (ac) drive field. We find that the glass freezing temperature T_g also shows $(x - x_c)^{½}$ type composition dependence (see inset of Fig. 9.6) with a better fit as compared to that for T_c at 300 kHz shown in the main figure.

9.3.4 Evidence for Quantum Electric Dipole Liquid (QEDL) Phase

The dielectric permittivity of BFO is anisotropic with a value of $\varepsilon_c \sim 42$ and $\varepsilon_{ab} \sim 18.2$ along the c-axis and the ab-plane, respectively [14]. The QPE behaviour (i.e. increase in the dielectric permittivity followed by its approximate saturation below ~10 K) is shown by ε_c only due to softening of the transverse optical phonon mode of A_{2u} symmetry [16,128] imparting BFO a uniaxial character with dipoles aligned along the *c*-

axis. The value of dielectric permittivity of BFO in our case is ~33.67 at ~ 3 K which in effect corresponds to an average over a large number of randomly oriented polycrystalline grains each with ε_c ~ 42 and ε_{ab}~ 18.2. The ε_c of BFO increases with decreasing temperature and reported to saturate below ~10 K whereas the ε_{ab} decreases and saturates to a nearly constant value for T < 50 K [14]. This suggests that the temperature dependence of dielectric permittivity ε (T) of sintered polycrystalline BFO below 50 K would be essentially due to the temperature dependence of ε_c only and we can analyse the data to examine the critical exponents of undoped and doped BFO in the low temperature range up to 50 K. The Curie-Weiss temperature Θ_{cw}, obtained from the extrapolation of the linear region in Curie-Weiss plots upto ~ 40 K (see Fig. 9.9) is found to be negative for all the compositions in the range $0 \leq x \leq 0.1$ as expected for AFE correlations. The magnitude of Θ_{cw} increases with increasing Ca^{2+} content (see Fig. 9.10). Since T_c of BFO is ~ 2.91 K whereas $|\Theta_{cw}|$ is ~ 423 K, the frustration parameter $f = |\Theta_{cw}| / T_c$ is very high (~ 141) and lies in the range where quantum spin liquid phase has been reported in the magnetic systems [40,62].

One of the criteria used to define a QSL phase in magnetic systems is linear temperature dependence of specific heat at low temperatures [62,151,478,483]. The temperature dependence of the specific heat of BFO from 1.8 K to 300 K is shown in Fig. 9.11. The specific heat plot does not reveal any sharp anomaly around T_c = 2.91 K, expected for a phase transition to a LRO AFE phase or glassy freezing, as can be seen more clearly from the inset of Fig. 9.11 on a magnified scale. However, C_P varies linearly with temperature dependence in the 1.8 to 2.5 K temperature range below T_c with a knee around 3.5 K. Such a linear temperature dependence of specific heat points towards the QEDL state in close analogy with QSL state [62,151,478,483]. Even after application of

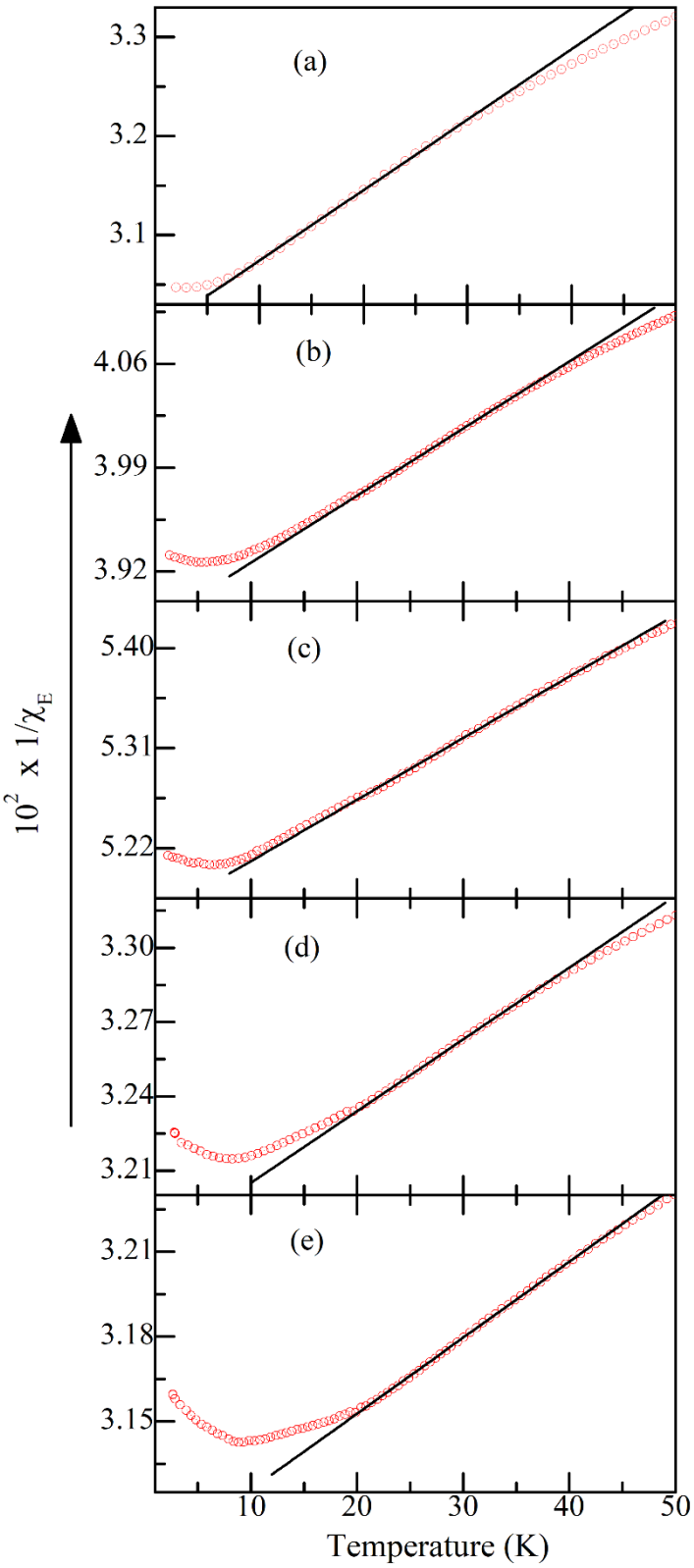

Figure 9.9: Curie-Weiss fit (black solid line) to temperature dependent permittivity (red circles) of $Ba_{(1-x)}Ca_xFe_{12}O_{19}$ for x = (a) 0.00, (b) 0.03, (c) 0.05 (d) 0.70 and (e) 0.10.

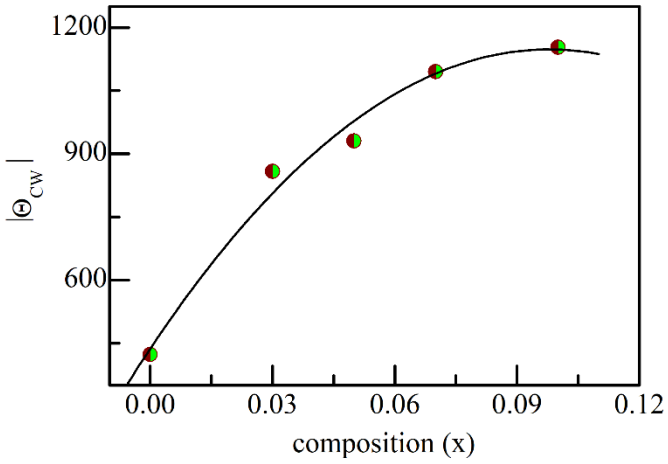

Figure 9.10: Variation of the magnitude of Curie-Weiss temperature $|\Theta_{cw}|$ of $Ba_{(1-x)}Ca_xFe_{12}O_{19}$ with concentration (x).

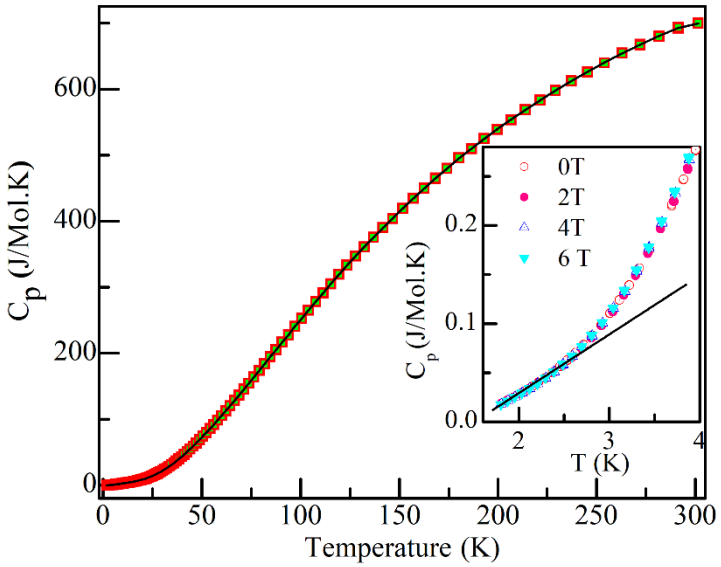

Figure 9.11: Specific heat of $BaFe_{12}O_{19}$ as a function of temperature. Inset depicts the specific heat measured at different fields on a magnified scale.

magnetic fields up to 6 T, we did not see any departure from the linear behaviour suggesting that this feature is linked with electric dipoles only and not the magnetic spins of the lattice. The signature of QEDL state is better seen after subtracting the Debye lattice contribution at low temperatures (T^3 dependence) in this non-metallic system.

Since the underlying magnetic sublattice is predominantly ferrimagnetic with large magnetic moment, one expects a $T^{3/2}$ dependence for the magnetic LRO phase [484]. Taking both aspects together, the specific heat of BFO should exhibit $C_P = \alpha T^3 + \beta T^{3/2}$ type temperature dependence at very low temperatures. This was confirmed by the linearity of the $C_P/T^{3/2}$ vs $T^{3/2}$ plot shown in Fig. 9.12 in the temperature range 1.8 to 11.8 K. Using this fit, we subtracted the Debye contribution to obtain the non-Debye part which is shown in inset of Fig. 9.12. The non-Debye part of specific heat also shows a linear temperature dependence below the dielectric anomaly peak temperature $T_c \sim 2.91$ K of undoped BFO. The positive curvature at low temperatures may be due to the non-zero entropy in the ground state characteristic of a geometrically frustrated systems [62,361,483]. The linear temperature dependence of the non-Debye part of the specific heat below ~ 3 K is not of magnetic origin as it does not show any field dependence upto 6 T (see inset of Fig. 9.12). Magnetic field leads to a slight decrease in

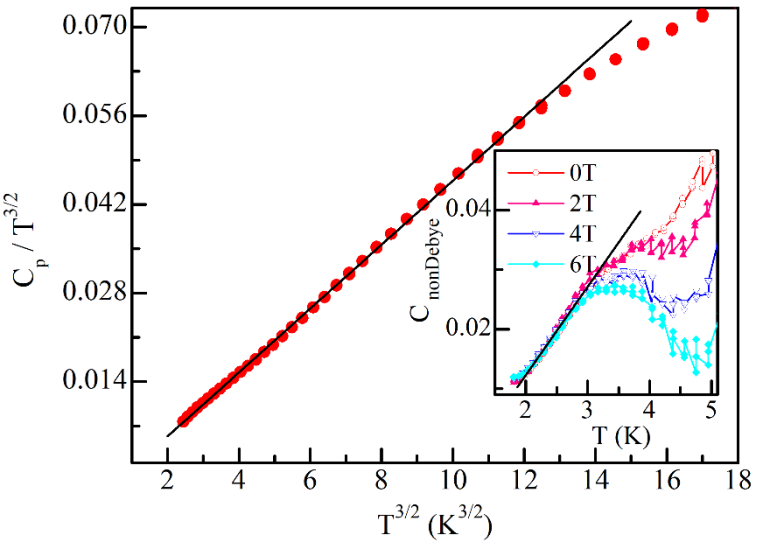

Figure 9.12: $C_p/T^{3/2}$ vs $T^{3/2}$ plot where solid line represents the linear fit. Inset shows the non-Debye part of the specific heat at different magnetic fields.

the specific heat above 3 K and transforms the step like feature of the non-Debye contribution of zero field measurement to a broad peak (see inset of Fig. 9.12). The frozen nature of the spins below the lowest temperature spin-glass transition temperature of about 5 K, discussed in chapter 5. These results imply that the spins below 3 K are already in place where they ought to have been and there is no scope for any change in the spin configuration unless the external field is sufficiently high such that $\mu_B H$ exceed the thermal fluctuation energy ($k_B T$) and/or zero-point fluctuation energy ($\hbar\omega_0$). Obviously, a field upto 6 T is not sufficient to disturb the spin configuration below 3 K. The field dependence of the specific heat above 3 K, on the other hand, suggests that $\mu_B H > k_B T/\hbar\omega_0$ for the applied fields which can therefore bring about change in the spin configuration.

The linear temperature dependence of specific heat and its field independence point towards the existence of a QEDL state below 3 K, although more work is required at much lower temperatures to confirm this proposition. The excess specific heat of non-Debye and non-magnetic origin clearly suggests the presence of low energy excitations. Several liquids and glasses reveal the presence of a Boson peak [267,269,271–275,279] in the C_P/T^3 versus T plots which has been taken as a signature of the presence of low energy localised excitations. This plot for BFO, shown in Fig. 5.18, and reproduced here as Fig. 9.13 in the 1.8 K to 20 K range, reveals the presence of two peaks. The higher temperature peak is related to the lowest temperature transverse spin-glass transition, and therefore not a typical Boson peak, as already discussed in chapter 5, whereas the lowest temperature peak around 2.7 K is due to the QEDL state. The existence of this peak suggests the presence of low energy localised excitations [271,277–285] which can not be modelled in terms of Debye theory for which C_P/T^3 should have been temperature independent. We hope that our results would encourage inelastic neutron scattering

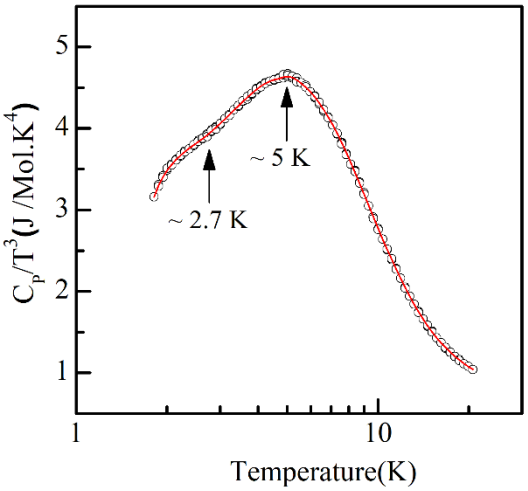

Figure 9.13: Boson peak at ~ 2.7 K in $BaFe_{12}O_{19}$

experiments with appropriate theoretical models to understand the origin of the Bose peak and the precise nature of these excitation associated with these peaks. Such a study in future may provide insight into the genesis of the QEDL state.

9.4 Conclusions

(1). We have showed that BFO exhibits a smeared dielectric response due to AFE correlations peaking at T_c ~ 2.91 K with a frustration parameter f ~141 from the temperature dependence of the dielectric constant.

(2). We have also presented results of specific heat measurements at different magnetic fields which suggest the possibility of a quantum electric dipole liquid state in this compound below T_c with a characteristics Boson peak around 2.7 K.

(3). We have investigated for the first time the quantum critical behaviour of BFO by driving it away from the QCP through a non-thermal variable, namely positive chemical pressure generated by Ca^{2+} substitution.

(4). Using Rietveld analysis of SXRD data, we have shown that the unit cell volume decreases with increasing Ca^{2+} content (x) confirming positive chemical pressure generated by Ca^{2+} substitution.

(5). Our dielectric measurements reveal that the chemical pressure generated by Ca^{2+} substitution stabilises a quantum electric dipole glass state whose glass transition temperature (T_g) follows $(x - x_c)^{1/2}$ type of composition dependence expected for a quantum phase transition. Our results reveal that BFO is close to its QCP but not quite at it. It would be interesting to investigate the behaviour of BFO under negative chemical pressure to reach its QCP as closely as possible experimentally.